

<https://doi.org/10.1038/s44172-024-00257-6>

Superalloys fracture process inference based on overlap analysis of 3D models

Check for updates

Xuecheng Zhang ^{1,2,4}, Guanghao Guo ^{3,4}, Zixin Li ^{1,2}, Wenchao Meng ¹✉, Yuefei Zhang ³✉, Qing Ye ¹, Jin Wang ³, Shibo He ¹, Xinbao Zhao ³, Jiming Chen ¹ & Ze Zhang ³

Superalloy materials exhibit susceptibility to fracture failures stemming from the influence of thermomechanical factors. To comprehensively understand the fracture mechanisms, material properties, root causes of failure, and the subsequent optimization of alloys, a detailed analysis of the internal fracture process and the morphological traits of the fracture surface is imperative. Traditional analysis of fracture surfaces solely relies on 2D images, thus lacking crucial 3D information. Although *in situ* experiments can capture the fracture process, their effectiveness is confined to the specimen's surface, precluding insight into internal changes. Here we introduce an integrated framework encompassing the process of 3D reconstruction of fracture surfaces, aiming to enhance the visual information obtained with micron-level accuracy, visual intuitiveness and sense of depth. Additionally, this framework also facilitates the scrutiny and inference of internal fracture processes. These results demonstrate that under specific service conditions, material deformation fracture probably stems from a combination of surface cracking and internal cracking rather than exclusively one or the other. Overall, our description and analysis of internally initiated cracking due to defects within the specimens can be beneficial in guiding future alloy design and optimization efforts.

Superalloys have gained notable prominence in the aerospace and energy fields^{1,2} due to their advantageous properties such as high-temperature strength, oxidation and corrosion resistance, fatigue properties, and notable fracture toughness^{3,4}. Analysis of fracture processes in superalloy specimens is of critical importance^{5–7} in the field of superalloy research. When an alloy specimen fractures, it results in two matching fracture surfaces, and the study of their appearance⁸ and location holds great value. The fracture phenomenon typically occurs in regions of the metal with the least strength, and the analysis of the fracture process is useful^{9,10} for gaining insights into mechanical and thermal properties and corrosion resistance of superalloys in extreme environments^{11,12}, such as high temperature and high pressure⁹. Deep insights can be obtained through detailed analysis of the fracture morphology, structure, and composition of superalloys. Researchers use this as a basis to guide the design of superalloy materials to enhance their strength and plasticity, further applying them to manufacturing and applications¹³.

Typical fracture analysis methods for superalloys include optical microscopy (OM)^{14,15}, scanning electron microscopy (SEM)^{16,17}, x-ray diffraction (XRD)^{18,19}, energy dispersive spectroscopy (EDS)^{20,21}, et al.

Appropriate methods and equipment selection depend on the actual needs and research objectives. Among all these methods, SEM has become an essential instrument for analyzing fracture surface morphology and microstructure due to its high resolution, considerable depth of field, and good stereoscopic effect²². SEM can directly observe the very rough surface of the specimen as well as the raw fracture of the material. The imaging principle of SEM is that the electron beam excites various physical signals on the specimen surface, such as secondary electrons(SE) and backscattered electrons(BSE), and these signals are acquired through the corresponding detectors to form an image²³. SEM images are, however, only two-dimensional (2D) intensity maps of the scattered electrons, and lack inherent three-dimensional (3D) information²⁴. This may lead to misinterpretations about the surface morphology of the specimen, as the 2D images do not accurately represent the true 3D nature of the specimen²⁵. For instance, in metallic materials, 2D images of grain and grain boundary morphologies are commonly depicted as polygons, while their 3D representations exhibit complex and irregular polyhedral geometries. To address this limitation, a suitable method for supplementing the 3D information of the specimen fracture surface is required^{13,26}.

¹State Key Laboratory of Industrial Control Technology, College of Control Science and Engineering, Zhejiang University, Hangzhou, 310027, China. ²Polytechnic Institute, Zhejiang University, Hangzhou, 310015, China. ³Institute of Superalloys Science and Technology, School of Materials Science and Engineering, Zhejiang University, Hangzhou, 310027, China. ⁴These authors contributed equally: Xuecheng Zhang, Guanghao Guo. ✉e-mail: wmengzju@zju.edu.cn;

yfzhang76@zju.edu.cn

Reconstructing 3D models from 2D SEM images has emerged as a prominent research area in microscopy. This approach improves the visual representation of the analyzed micro-objects and increases the accessibility of measurable data. The acquisition of a 3D model can be broadly categorized into two types, namely, destructive, and non-destructive, depending on the extent of potential damage caused to the specimen.

Destructive techniques such as serial block-face imaging (SBF)²⁷, metallographic serial polishing (MSP)²⁸ and focused ion beam (FIB)²⁹ capture layer-by-layer images of the specimen and thus such a process is irreversible. These techniques share the standard approach of capturing layer-by-layer images of the specimens, yet the process is irreversible. Careful selection of appropriate slicing methods based on the specimen and the research criteria is crucial, ensuring minimal damage while managing cost, time, reconstruction scope, and accuracy considerations. Furthermore, these techniques are better suited for reconstructing within cuboid regions, but they are not ideal for objects such as fractures with substantial surface profiles.

Standard non-destructive testing techniques in structural analysis encompass X-ray computed tomography (CT) and the utilization of 3D computer vision algorithms to analyze and process 2D images. CT technology allows for acquiring a sequence of cross-sectional images of the specimen through non-invasive tomographic scans, which are then amalgamated to form a 3D structural model for internal assessment³⁰. Nevertheless, CT technology is constricted by radiation exposure, high expenses, and limited resolution. In contrast to in situ SEM observations, CT outcomes lack morphological details, rendering them more applicable for quantitative evaluations of structural volume but less convenient for multi-scale observations. Techniques utilizing 3D computer vision algorithms to analyze and process 2D images³¹ offer the notable advantage of preserving the integrity of the specimens and facilitating subsequent analysis. Furthermore, it enables a broader reconstruction scope and faster speed^{13,32-34}.

Among these methods, 3DSEM, based on the photogrammetric reconstruction of SEM images, is widely adopted due to its low cost and ease of use³⁵. The technique involves capturing images from multiple perspectives by moving the detector around the specimen or rotating and tilting the specimen within the field of view^{36,37}. This capability is particularly suitable for reconstructing the surfaces of specimens with marked variations, such as fractured specimens. Identifying and matching features in these images enables the calculation of a point cloud, which is further used to generate a surface model. Post-processing techniques, including noise reduction, smoothing, and repair, are applied to the surface model to improve the accuracy of the 3D model^{38,39}. However, this method has certain limitations. For instance, the model's completeness directly relies on the availability of comprehensive feature information on the fracture surface and the specimen surface in the original images. Therefore, enhancing the data acquisition method is necessary to obtain additional height feature data for complex features. In addition, unlike traditional photogrammetric techniques, the electronic microscope images on which this method is based lack information about the camera's internal and external parameters during the imaging process. Consequently, the overall dimensions of the resulting 3D model may need to be more accurately scaled up or down in proportion.

In this work, we introduce an innovative framework to infer the superalloy fracture process, utilizing 3D model overlap analysis to examine the deformation failure progression in alloy specimens. Notably, our 3D fracture morphology models are reconstructed exclusively from SEM images, thus effectively controlling expenses, and simplifying the operational procedure. These 3D fracture morphology models provide a comprehensive representation of the morphology and intricate details of the specimens in 3D space, overcome difficulties related to cross-section matching and boundary information observation, and include precise dimensional information. Different fracture regions exhibit variational extension during tensile deformation due to differing stress durations. Overlap analysis of the individual 3D fracture morphology models is carried out to elucidate the comprehensive internal fracture mechanism of the specimens. Our results reveal a characteristic material deformation pattern, highlighting the interplay between surface cracking and internal fissures, challenging the notion of these

phenomena as isolated occurrences. These conclusions have been subsequently verified and detailed through in situ experiments, showcasing practical and innovative advantages in real-world applications.

Results

Framework of SFPI

We develop a superalloys fracture process inference (SFPI) framework consisting of multiple steps (Fig. 1). The framework aims to reconstruct 3D models of the fracture surface of experimental specimens after tensile testing and provide a comprehensive observation and inference of the fracture process. We conducted in situ tensile experiments on two IN718 specimens at room temperature (RT) and 650 °C high temperature (HT). After conducting the in situ experiments, we proceeded with the 3D reconstruction and scale calibration of the fracture surfaces, which yielded 3D models named Fracture A and Fracture B after the HT in situ tensile testing, as well as 3D models named Fracture C and Fracture D after the RT in situ tensile testing.

After obtaining 3D models featuring precise dimensional discontinuities, the next step involves aligning these models to achieve a multi-surface stereoscopic observation, enriching the visual data and ensuring accurate scale information. To address the challenges posed by varying extension rates in different regions during the stretching deformation process, a periodic overlap and separation strategy is employed for the corresponding 3D models. The periodic overlapping and separation of these models reveal internal regions of the specimen, offering insights into the chronological sequence of events during the fracture process. In Table 1, we provide a comparative analysis of our proposed method with current standard materials characterization and analysis techniques. As a result, our innovative research involves previously inaccessible details about the specimen, including temporal evolution scales, a feat unattainable through other existing methodologies.

Multi-surface stereoscopic observation

For traditional material fracture analysis, matching and seamlessly integrating fracture surface and edge morphology is often necessary to comprehensively examine fracture processes and mechanisms. However, this practice gives rise to two distinct challenges. The first challenge is that the researcher manually matches the SEM images of the fracture surface and the specimen surface to accurately compare and integrate the morphological information. This task is laborious and subjective, leading to biased evaluation results. The second challenge is that analyzing the microstructure at the interface between the specimen and fracture surfaces requires the researcher to rely on their experience and knowledge. Furthermore, the microstructure information, vital for the fracture analysis, must be reconstructed from 2D images, leading to inherently subjective judgments and prone to substantial errors, ultimately lacking in objective credibility. These challenges primarily stem from the inherent limitations of 2D images, which represent planar projections of 3D materials, thereby necessitating a richer spatial dataset for a more comprehensive analysis.

The fracture models offer a more intuitive depiction of the specimen's overall morphology and specific details in 3D space (Fig. 2). Each fracture model comprises a cross-section and four side surfaces. We can observe the information from ten surfaces by aligning the corresponding fracture models. This integration of multidimensional material features provides a more comprehensive and precise visual depiction, particularly emphasizing the morphological attributes at the interface and the elevation within the plane. Fracture A and Fracture C in Fig. 2 demonstrate that our model, as it incorporates both surface and fracture morphology, enables researchers to analyze these characteristics without tedious comparisons efficiently, ultimately enhancing the accuracy of the analysis process. The model exhibits distinct microscopic organizational structures at the interface junction, as denoted by the white arrows, which are not observable in conventional 2D SEM images.

By leveraging these inherent characteristics, it is possible to provide a more comprehensive and accurate description of the typical positions of deformation and the mechanisms of fracture that occur during the process of material fracture. For instance, in the case of the IN718 HT tensile test

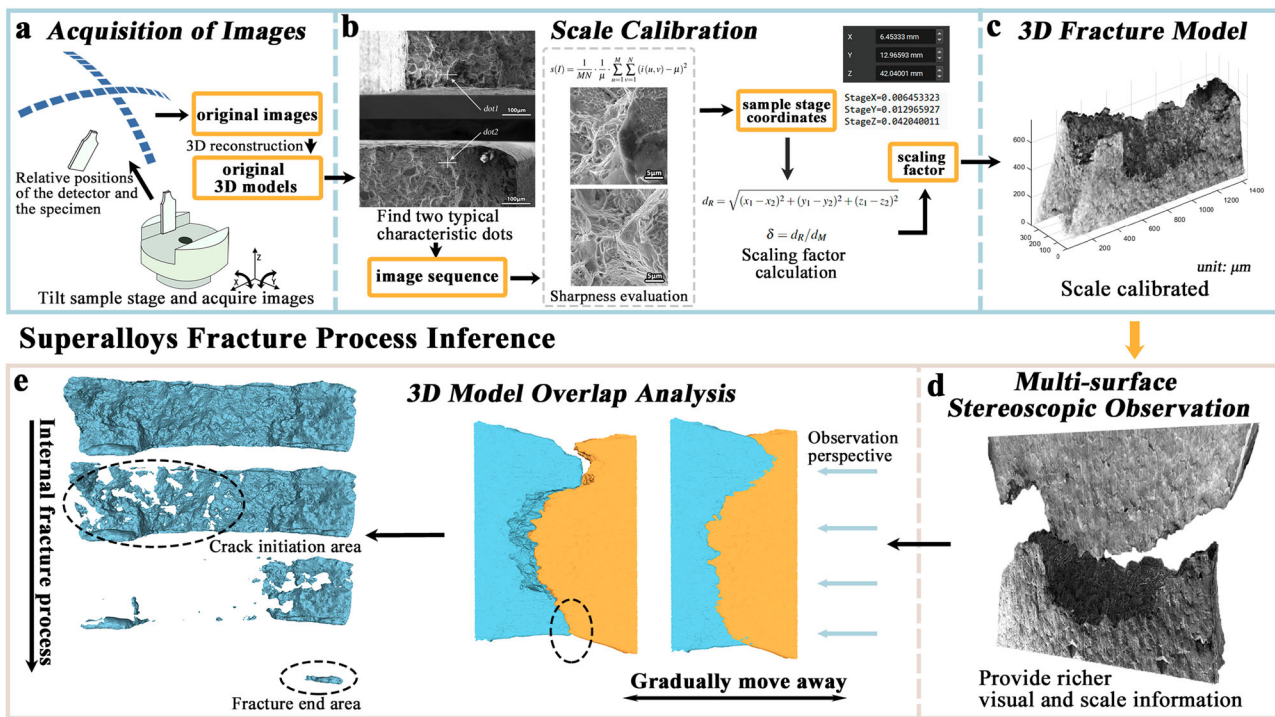


Fig. 1 | Overview of the proposed superalloys fracture process inference framework. **a** Improved image acquisition process. Images of the fracture specimens from different viewpoints were obtained by tilting the sample stage, and 3D reconstruction was performed to obtain the original 3D models. **b** Calculate the scaling factor to complete the 3D model scale calibration through image sharpness evaluation. **c** Calibrated 3D fracture morphology model in 3D coordinate system. **d** Multi-

surface stereoscopic observation. Simultaneous observation of multiple surfaces through a pair of 3D fracture morphology models to solve problems such as difficulty in matching boundary features. **e** The internal fracture process of the sample was obtained by inferring from the 3D model overlap analysis. The figure shows the area where the internal cracking starts and the area where the fracture ends.

Table 1 | Proposed method compared with other methods of material characterization and analysis

Method	Proposed	In situ SEM observation ^{2,3,45}	In situ X-ray diffraction ^{19,53}	Layer-by-layer slice ²⁷⁻²⁹
Non-destructive	✓	✓	✓	
3D feature	✓		✓	✓
Scale information	✓	✓	✓	✓
Time dimension information	✓	✓	✓	
Internal observation	✓		✓	✓
Morphology information	✓	✓		✓
Multi-scale observation	✓	✓		

specimens, the surface patterns of Fracture A and Fracture B consist of interlocking zig-zag shapes. The cross-section analysis reveals a higher presence of intact grains, indicating that the primary fracture mechanism is intergranular fracture (Fig. 2e). Conversely, the surfaces of Fracture C and Fracture D of the IN718 RT tensile test specimens exhibit a smoother appearance, suggesting that the dominant fracture mechanism in these cases is transgranular fracture (Fig. 2f). The proposed method offers an improved spatial representation of material properties by providing 3D information. This renders it a valuable research tool for the analysis of material fractures.

Reconstruction performance analysis of 3D models

The 3D fracture morphology models allow for precise visual observation of the cross-sectional profiles of fractures and the morphology and roughness of the four side surfaces. Furthermore, it facilitates the precise measurement of grain size, ligamentous fossa depth, and other critical parameters. In order to validate the accuracy of the 3D fracture reconstruction model, we

employed a hardness tester to create two indentations spaced 500 μm apart along the horizontal direction on one side surface of Fracture A prior to reconstruction. After reconstruction, we measured the distance between the centers of the two indentations using the measurement tool in Meshlab software in the reconstructed 3D model and compared it with the standard value, obtaining an error of less than 1% (Fig. 2a).

The above method can verify the model's accuracy. In addition, two specific cases have been highlighted to better demonstrate the effectiveness of the three-dimensional cross-sectional model in achieving precise measurement and comprehensive observation. The first figure in Fig. 2g shows the distance between two diagonals of grain in the original SEM image of Fracture A, measured using the distance measurement function in Tescan Essence S9200X Demo software, which is 29.16 μm . In the second figure in Fig. 2g, the distance between two diagonals of the exact grain in the 3D model within the same perspective was measured using the measurement tool in the Meshlab software (v2022.02), which is 30.1396 μm , slightly larger

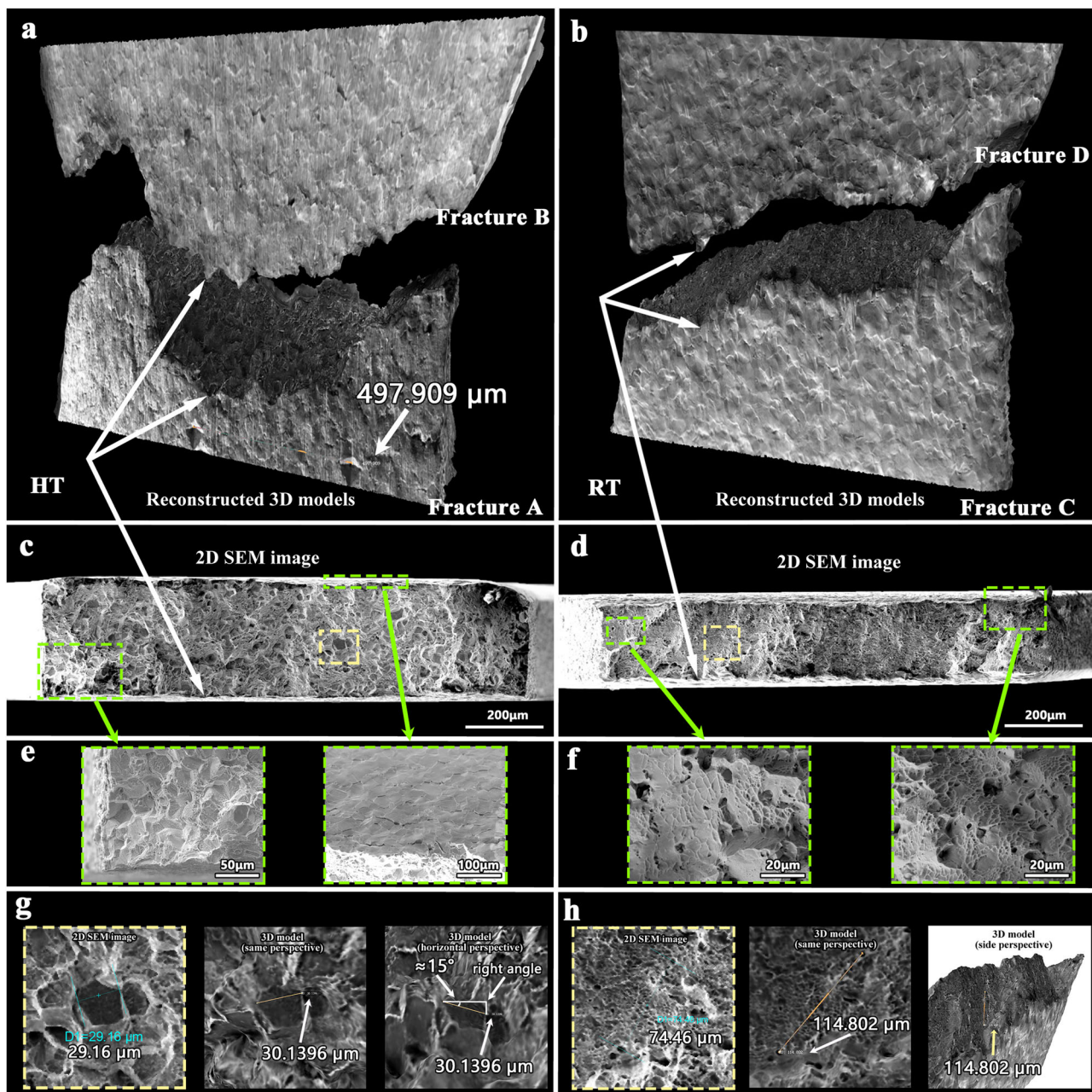


Fig. 2 | Comparison of 2D images and 3D stereoscopic observation and verification of scale calibration results. **a, b** 3D fracture surface models of IN718 after 650 °C high temperature (HT) and room temperature (RT) tensile experiments with an indentation spacing in the model. **c, d** Corresponding 2D Scanning Electron

Microscope (SEM) images of the fracture surface. **e** Intergranular fracture at 650 °C. **f** Transgranular fracture at RT. **g** The distance between two diagonals of grain in an SEM image and a 3D fracture morphology model. **h** The distance between two void defects in an SEM image and a 3D fracture morphology model.

than the value in measured in SEM image. The difference in the number of decimal places in the two sets of measurement results is due to the use of different measurement software. By changing the viewing angle of the 3D model, it can be determined that the reason for this phenomenon is the surface of the grain is not horizontal but has a certain inclination angle. The distance measured in the 2D SEM image is the projection of the actual distance in the horizontal direction. The actual distance between the two characteristic points should be calculated by dividing the distance measured in the 2D SEM image by the cosine of the angle θ formed by the line connecting the two points and the horizontal plane. For the selected grain, the angle θ between the two diagonal lines and the horizontal direction is approximately 15°. The measurement error induced by this angle is not apparent in SEM images but is relatively more precise in the 3D model.

Figure 2h provides a more definitive example employing the same methodology. In the SEM image of Fracture C, the measured distance between the two void defects is significantly less than the distance measured from the 3D model. This discrepancy is attributed to the substantial angle between the fracture surface of the sample and the viewing perspective, further demonstrating the superiority of 3D stereoscopic observation.

The model effectively reconstructs the microstructure, reflecting the actual physical information of the material on the fracture surface. The currently obtained 3D model accurately represents the spatial and physical scales, offering precise references for further research. In order to obtain more detailed information, the resolution and clarity of the original SEM images can be enhanced, although it will also lead to increased computation time.

Inference of the fracture process

Many experimental studies on IN718 tensile properties have revealed that the fracture process is usually in transgranular mode at RT due to the stable crystal structure and uniform strain distribution^{40,41}. At HT, a more significant number of grain boundary cracks appear as a result of reduced interfacial strength. In addition, as the experimental temperature rises, more slip and other localized deformations will occur within the specimens, leading to uneven deformation in the local regions of polycrystalline materials. However, this analysis is based solely on inferred material fracture morphology analysis, lacking direct visualization and objectivity.

In this work, we have reconstructed and calibrated fracture models for IN718 at both RT and 650 °C. It is important to note that the two fracture surfaces were obtained from *in situ* tensile experiments, which allows for observing surface morphology evolution during the tensile process. During the tensile deformation process, local stress concentrations arise in the material due to the incomplete uniformity of grain orientation and size and the presence of second-phase particles^{42,43}. This results in the preferential

cracking of certain grains characterized by reduced elongation. The non-cracked regions experience axial load and further elongate during subsequent stretching. As a result, the fracture surface exhibits varying elongation rates across its local features, rendering complete macroscopic alignment unachievable. Ultimately, the portion that fractures finally exhibits the highest elongation rate, resulting in its initial contact during the alignment process, while the initially cracked parts remain the farthest apart. We inferred the tensile deformation process of the specimens by constructing 3D fracture morphology models and considering the perspective of material fracture.

Our inference method, combined with the model morphology from a fractured perspective, allows for a detailed analysis of the dynamic process of IN718 tensile deformation at both RT and HT. Figure 3 illustrates the inference results of the two sets of experiments, with each image showing a projection of the overlapping portion of the fracture models at different tensile displacements. This overcomes the limitations of traditional fracture analysis and facilitates a transition from traditional inferential analysis to a

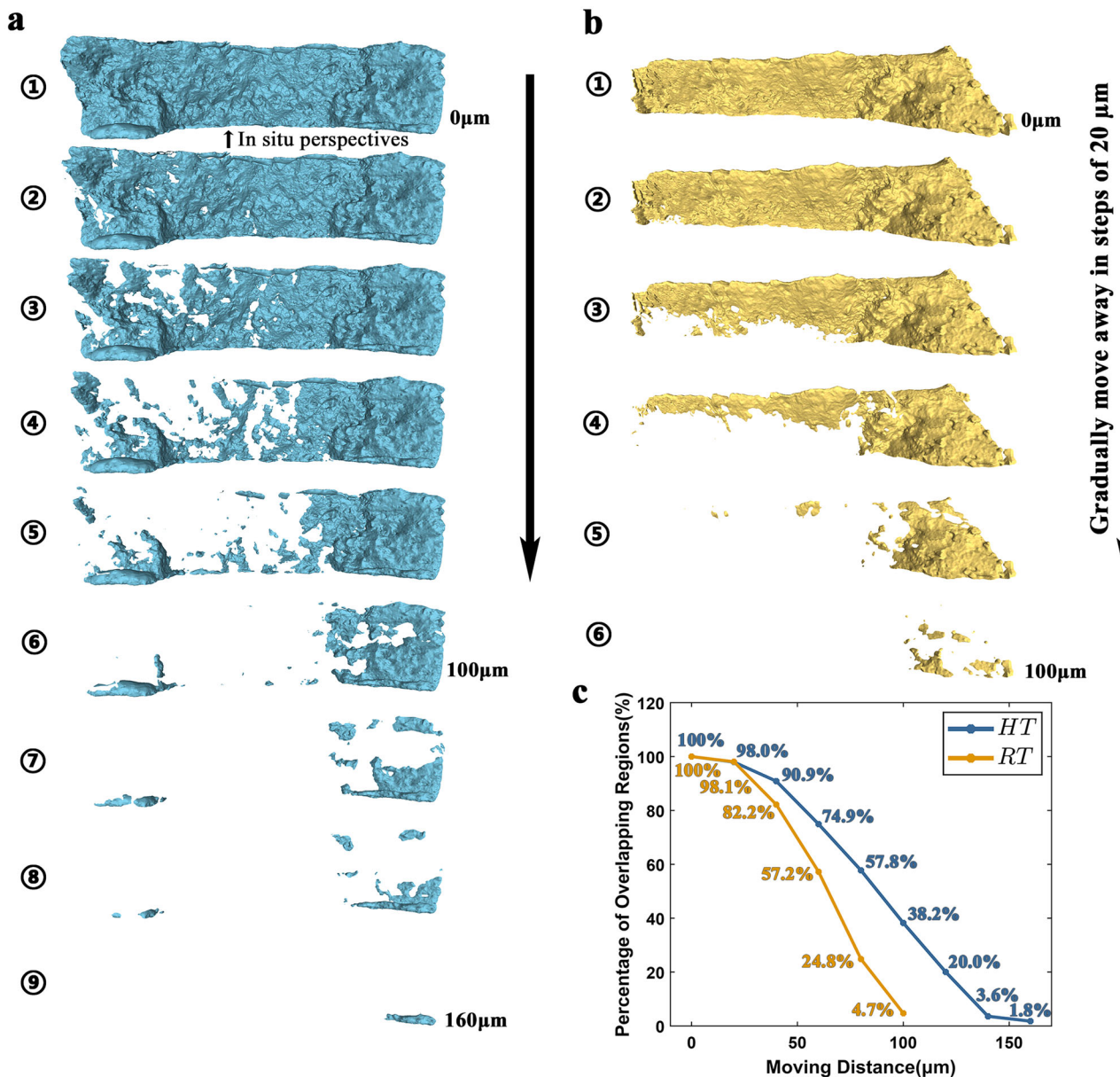


Fig. 3 | Inferred results of specimens fracture processes in IN718 650 °C high temperature (HT) and room temperature (RT) tensile experiments. **a** Results of HT fracture process inference. **b** Results of RT fracture process inference. **c** Statistical

analysis of the ratio of crack area between the results of HT and RT fracture process inference under different stretching displacements.

more intuitive visual observation. By comparing Fig. 3a and b, it becomes evident that there are substantial differences in material cracking between RT and HT tensile deformation. There are more localized plastic cracking regions with smaller areas in HT conditions, indicating that the local non-uniform deformation phenomenon is more evident. This observation is also consistent with traditional theory.

In RT fracture process inference results, the transition from localized cracking to final fracture occurs at a tensile displacement of 100 μm . Conversely, in the HT fracture process inference results, this transition occurs at a more extended tensile displacement of 160 μm . Furthermore, Fig. 3c comparison reveals that RT tensile deformation results in a larger cracking area (overall statistical area) under the same strain, indicating poorer plasticity. This phenomenon cannot be directly observed through traditional fracture analysis techniques. Through the overlap analysis method of the 3D model, the observation and analysis of the fracture process become more intuitive and accurate, effectively solving the limitations of the traditional theory. With further improvements in spatial resolution, it can also be widely used for more microscopic observations and analysis.

Description of the internal fracture process and comparison with in situ experiments

When grain deformation occurs in polycrystalline materials, it will coordinate deformation with surrounding grains. Researchers categorize grains into internal and external grains based on their positions as they experience

distinct mechanical constraints⁴⁴. Surface grains possess certain free surfaces. Comparatively, fewer grains deform in coordination. Thus, the contributions of these two-grain types to mechanical deformation are different.

Based on the discussion in the previous section, it has been identified that the tensile fracture of the material is not limited to simple surface or internal cracking but rather involves a comprehensive combination of both. Traditional fracture offset analysis fails to provide a direct understanding of the deformation process, while in situ SEM characterization solely captures the evolution of surface morphology. The method proposed in this paper not only focuses on surface evolution but also simulates the occurrence of internal cracking. This allows for precise determination of the fracture location, whether it emerges internally or on the surface. Notably, previous methodologies have been unable to accomplish this.

According to the results of the HT fracture process inference, we have selected four regions within the specimen that experienced cracking first to describe further. Figure 4 displays a scanning image of Fracture A, highlighting the four selected regions using different colored circles. It can be observed that Region 1 does not show any typical defects. However, a crack is visible at the corresponding position on the opposite side of the fracture surface, potentially leading to cracking within the specimen. Similarly, Region 4 exhibits a comparable scenario, wherein multiple void defects can be observed at the corresponding position on the opposite side of the fracture surface. An inclusion is detected within Region 2. Further analysis using EDS reveals it is a titanium compound. Furthermore, Region 3 directly

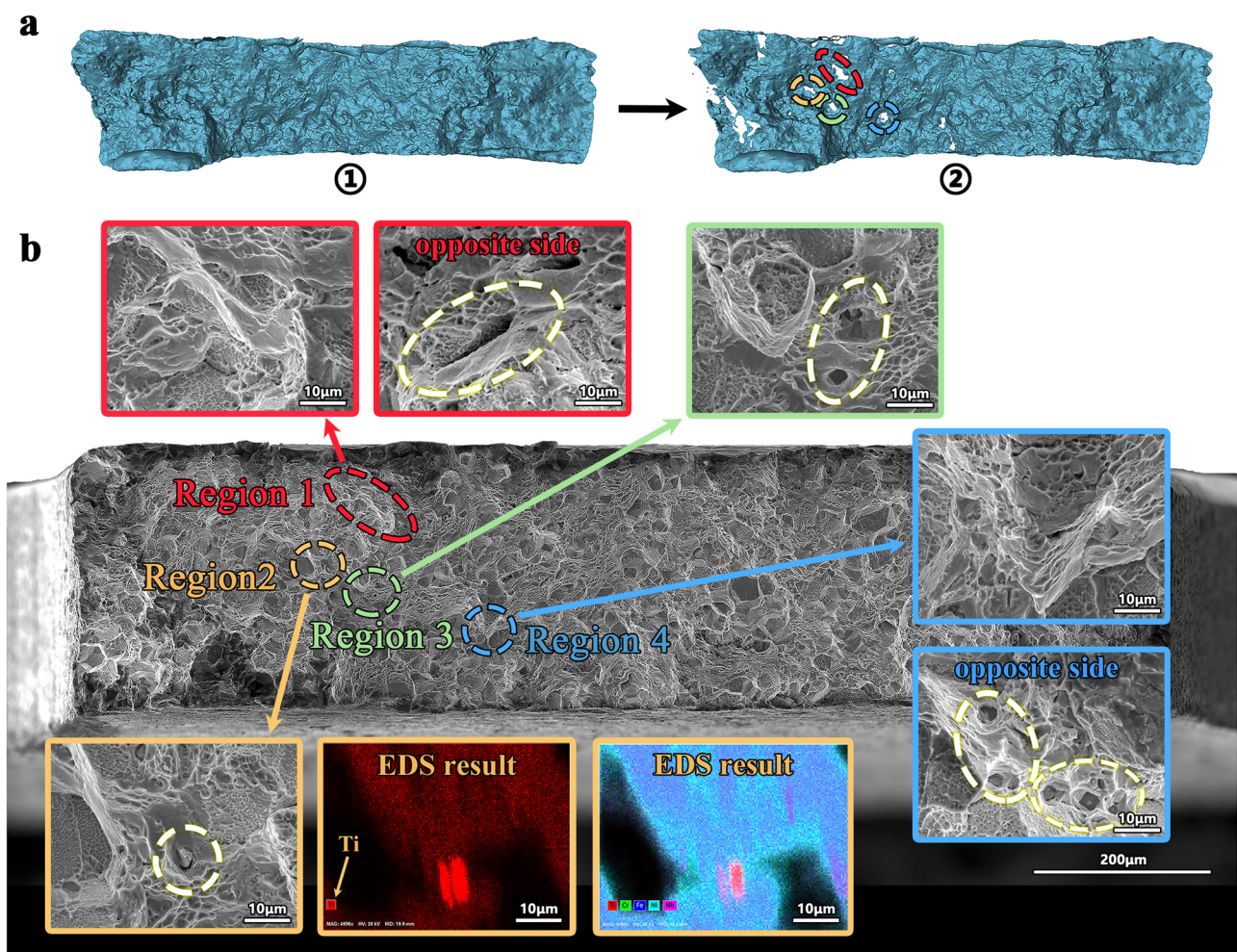


Fig. 4 | Description of internal cracks. **a** Based on the results of 650 °C high temperature (HT) fracture process inference, four regions were randomly selected for further analysis. The four regions are distinguished by different colors. **b** Scanning electron microscope (SEM) images of fracture A and four regions are shown along

with additional images to illustrate internal defects. The opposite side in the additional images of Region 1 and Region 4 indicates the corresponding position of the images acquired in Fracture B. The additional images of Region 2 indicate the results of the energy dispersive spectrometer (EDS) analysis.

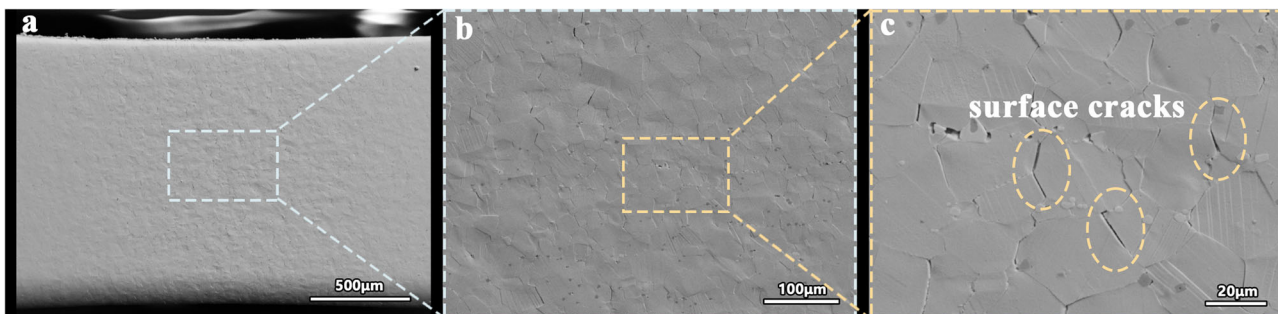


Fig. 5 | The morphology of surface cracks occurring during the in situ experiment under 650 °C high temperature (HT) tensile conditions. **a** 200x. **b** 500x. **c** 2kx.

displays two void defects. The dimples in the fracture surface images indicate significant plastic deformation within these regions, which is manifested macroscopically as excellent ductility. These defects may precipitate the initiation of cracks in these regions during tensile testing. Notably, the observed defects correspond to the regions where initial cracking was identified during the fracture process analysis, thereby enhancing the credibility of the overall inferential process. These findings, which rely on this study's fracture model and analysis method, offer compelling evidence of their distinct advantages and crucial significance in material fracture research.

In addition, we provide a detailed analysis of the distinct deformation processes of surface grains and internal during the tensile deformation of IN718 by comparing the results with the in situ experiments, with the results of HT fracture process inference serving as an illustrative example. The fracture process inference results depicted in Fig. 3 demonstrate that cracks occur at a strain of 140–160 μm before the specimen's final fracture strain. During the in situ experiment, images were captured to document the deformation length of the specimen. Figure 5a–c depicts the morphology of surface cracks occurring during the in situ experiment under HT tensile conditions. Notably, surface cracks (precisely grain boundary cracks) were observed to occur at 110 μm of strain before the strain reached the final fracture strain of the specimen under HT conditions. This suggests that internal cracking occurs before the manifestation of surface cracks, a phenomenon not previously observed in direct material observations. These empirical findings demonstrate the substantial distinction between surface and internal grains. Additionally, it implies that the surface phenomena observed through in situ SEM exhibit a delay compared to the actual material deformation.

Discussion

This study delves into advanced methodologies dedicated to unraveling the intricate superalloy fracture processes through the comprehensive analysis of overlapping 3D models. We introduce and implement an optimized image acquisition scheme tailored for the three-dimensional reconstruction of SEM images. The resulting calibrated 3D models not only endow our alloy fracture analysis with a wealth of visual details but also ensure a high degree of precision in scale information. By meticulously analyzing these overlapping 3D models, we can infer the initial position of specimen cracking and the evolution of crack paths during the tensile process. Our findings reveal a notable insight: under HT tensile experimental conditions, it is probable that internal defects within the specimens lead to internal cracking before surface cracking. This discovery aligns seamlessly with the outcomes of our in situ experiments, corroborating its validity. Looking ahead, this speculative methodology holds great promise for enriching our understanding of alloy fracture mechanisms, consequently facilitating the design and optimization of alloy performance. Furthermore, we acknowledge the challenges and opportunities ahead, particularly in the realms of enhancing the clarity of 3D fracture morphology models and advancing in situ 3D reconstruction techniques, both of which will considerably shape the trajectory of our future research efforts.

Methods

In situ tensile testing and reconstruction of 3D fracture morphology models

Two sets of in situ tensile experiments on IN718 were conducted to address specific issues. The in situ tensile specimens were designed in a dog-bone shape with a unique structure to enable easy observation during the experiments. Comprehensive information about the composition of the materials (Supplementary Tables 1–2), processing techniques, dimensions and structure of the specimens (Supplementary Fig. 1), and corrosion treatment can be found in the Supplementary Information.

The equipment used for conducting in situ tensile testing was developed by our research group and has been extensively described in previous work^{2,45}. The concrete figure and the schematic cross-section of the working parts of the experimental equipment are shown in Supplementary Fig. 3–4. The testing equipment facilitates in situ tensile testing ranging from RT to 1200 °C, meeting high-resolution SEM image acquisition requirements. The experimental conditions and data results strongly support the findings of this research. Two specific sets of in situ tensile experiments were conducted: RT testing and on 650 °C IN718. Each set of in situ uniaxial tensile experiments was conducted at a constant tensile rate of 1 $\mu\text{m}/\text{s}$ until fracture was evident. Real-time changes in the morphology of the SEM images are continuously monitored during the tensile process. Photographs are captured at distinctive intervals to record the corresponding displacement in the tensile curve. HT tensile testing at 650 °C necessitates a gradual temperature increase to a specific level, followed by a 30-minute dwell time to minimize temperature fluctuations and non-uniformity in the pre-marked section before the actual tensile testing. These details have been thoroughly elaborated on in previous studies and have reached a high level of applicability^{3,45}.

In the 3DSEM³⁵, images are obtained by tilting the sample stage to a fixed angle and capturing images at different angles by rotating the stage. However, this approach results in information loss due to surface features on the fractured surface, which resemble peaks and valleys and are more sensitive to gradient information. To address this concern, we propose an optimized method for image acquisition (Supplementary Fig. 5a), where tilting is employed instead of rotating the sample stage. In this method, the specimen is fixed on the stage inside the SEM chamber, and the tilt angle and field of view are adjusted to achieve optimal focus and ensure a clear and centered view of the specimen cross-section.

Image acquisition was realized with a Tescan Mira4 SEM. Considering the reconstruction effectiveness and data collection efficiency, the image acquisition scheme applied in this article is as follows: the sample stage is tilted along the X-axis and the Y-axis, capturing images at 5° intervals within the -30° to 30° range. The relative positions of the detector and the specimen throughout the image acquisition process are shown in Supplementary Fig. 5b. We used an SE detector to obtain 25 sets of raw image data at different angles, with each image being 2048×1024 pixels, and was saved in the TIF format. Throughout the entire image collection and reconstruction process, we only used Photoshop 2020 software to crop out the SEM information from the raw images and saved them in JPG format. The acquisition of the 3D model was achieved by processing the image sequence

using Agisoft Metashape software(v1.8.4) to complete the reconstruction process.

Since accurate camera parameters are not available in advance, the reconstructed 3D models are usually scaled up or down proportionally and thus require scale calibration. In order to obtain the scaling factor, standard measurement methods involve the use of other equipment, such as white light interferometers^{46,47}, white light chromatic sensors⁴⁸, and atomic force microscopes⁴⁹. However, cost and time control are difficult for objects with large volumes and characteristic features like alloy fractures. We propose a scale calibration method for accurate scale calibration and adjustment of 3D models using only SEM images.

We aim to identify two marked points in the cross-section on the fracture surface, *dot1* and *dot2* (Supplementary Fig. 6a), each exhibiting distinctive features. By utilizing a 10 kx magnification, we meticulously observe and optimize the focus of *dot1* to ensure image clarity. While maintaining a fixed focus, we incrementally adjust the height *Z* of the sample stage in 10 μm steps. This procedure allows us to capture a sequence of images that exhibit an increasing and subsequently decreasing level of sharpness (Supplementary Fig. 6b). We employ an identical method to obtain a sequential set of images for the position of *dot2*. Efficaciously, the entire process is completed in approximately 30 min.

Marturi^{50,51} et al. evaluated the efficacy of standard sharpness functions in accurately determining the clarity of SEM images. They identified that the normalized variance equation effectively balances speed and accuracy trade-offs. The formula employed for calculating the normalized variance, denoted as $s(I)$, is presented below:

$$s(I) = \frac{1}{MN} \cdot \frac{1}{\mu} \cdot \sum_{u=1}^M \sum_{v=1}^N (i(u, v) - \mu)^2 \quad (1)$$

where *M* and *N* are the length and width of the input image, respectively, $i(u, v)$ is the pixel intensity at coordinate (u, v) , and μ is the average intensity of all pixels in the input image.

The sharpness score curve for the two markers in Fracture A can be found in Supplementary Fig. 6c. It is important to note that the displacement of the specimen is equivalent to the displacement of the sample stage under a constant focal length, as they are fixed relative to each other. The 3D coordinates of the sample stage were determined at the point of highest clarity. Image sharpness assessment curves for four fracture models are shown in Supplementary Fig. 7. The distance d_R between *dot1* and *dot2* is:

$$d_R = \sqrt{(x_1 - x_2)^2 + (y_1 - y_2)^2 + (z_1 - z_2)^2} \quad (2)$$

where x_1, y_1, z_1 , and x_2, y_2, z_2 represent the XYZ axis coordinates of the sample stage when observing *dot1* and *dot2*, respectively.

$$\delta = d_R/d_M \quad (3)$$

Locate *dot1* and *dot2* in the reconstructed 3D model, and measure and calculate the distance d_M . Calculate the scaling factor δ using equation (3), and use the scaling factor to scale the final calibrated 3D model.

Superalloys fracture process inference method and validation

Using the overlap analysis of 3D fracture morphology models to infer the fracture process of specimens, the specific method proceeds: firstly, the corresponding fracture models are gradually brought together until they overlap entirely (Supplementary Fig. 8a). To observe the projection of the target fracture surface coinciding with the opposite fracture surface, it can be observed from inside the opposite fracture. The complete morphology of the target fracture surface can be seen when two fracture models are fully overlapped (Supplementary Fig. 8d). This stage signifies the connected state of the specimen during the actual tensile process prior to fracture initiation. Subsequently, a gradual distancing from the associated model occurs with a step size of 20 μm (Supplementary Fig. 8b). During the tensile process, the

region where cracking initiates displays a notch in the projection figure due to its reduced elongation rate (Supplementary Fig. 8e). With the increasing separation of the corresponding model, the cracking process, encompassing crack initiation, propagation, and ultimate fracture, become evident. After a separation distance of 160 μm , only the region within the black circle exhibits overlapping between the corresponding models (Supplementary Fig. 8c), indicating the location of the fracture termination (Supplementary Fig. 8f). The labeled distances in Fig. 3 represent the displacement at which the corresponding model gradually moves away, equivalent to the tensile displacement observed in actual tensile experiments. It should be noted that our analysis method assumes that all local material points follow a uniaxial tensile state.

To further validate the accuracy and effectiveness of the tensile fracture process inference, we conducted an additional analysis using in situ tensile experiments conducted on a new Ni-based wrought superalloy (NWS)⁵² specimen at RT. The material's fracture process becomes increasingly apparent as the deformation progresses. The position of the initial surface cracking coincides with the fracture process inference results, thereby providing robust evidence for the highly accurate fracture process inferred by our framework (Supplementary Fig. 9).

Furthermore, we employed our proposed methodology to reconstruct and analyze the ex-situ tensile fractures of circular cross-section specimens made of IN718 to validate the method's universality. Six typical stages of the fracture process inference are shown (Supplementary Fig. 10a). The original SEM images of the fractures are depicted, revealing the fundamental characteristics of the morphology (Supplementary Fig. 10b). However, they lack precise 3D perspective and quantitative analysis. Subsequently, the results of the 3D reconstruction and registration of the fractures are showcased (Supplementary Fig. 10c). The comparative study demonstrates the practical application of our methodology to circular section specimens' fractures, thereby affirming the universality of our framework.

Data availability

The source data and data folds in the four fractures of two specimens used in this study are provided on the Zenodo at <https://zenodo.org/records/10430093>.

Code availability

The source code for calculating image sharpness in SFPI is available on the Zenodo at <https://zenodo.org/records/10430093>.

Received: 22 January 2024; Accepted: 29 July 2024;

Published online: 06 August 2024

References

1. Shahwaz, M., Nath, P. & Sen, I. A critical review on the microstructure and mechanical properties correlation of additively manufactured nickel-based superalloys. *J. Alloy. Compd.* **907**, 164530 (2022).
2. Guo, G. et al. In-situ SEM-EBSD investigation of the low-cycle fatigue deformation behavior of Inconel 718 at grain-scale. *J. Mater. Res. Technol.* **24**, 5007–5023 (2023).
3. Sang, L. et al. In-situ SEM study of temperature-dependent tensile behavior of Inconel 718 superalloy. *J. Mater. Sci.* **56**, 16097–16112 (2021).
4. Jiang, W. et al. Study of pre-precipitated δ phase promoting deformation twinning and recrystallization behavior of Inconel 718 superalloy during hot compression. *Mater. Des.* **226**, 111693 (2023).
5. Hanson, J. P. et al. Crystallographic character of grain boundaries resistant to hydrogen-assisted fracture in nibase alloy 725. *Nat. Comm.* **9**, 3386 (2018).
6. Naragani, D. P., Shade, P. A., Kenesei, P., Sharma, H. & Sangid, M. D. X-ray characterization of the micromechanical response ahead of a propagating small fatigue crack in a Ni-based superalloy. *Acta Mater.* **179**, 342–359 (2019).

7. Griffiths, S. et al. Combining alloy and process modification for micro-crack mitigation in an additively manufactured Ni-base superalloy. *Addit. Manuf.* **36**, 101443 (2020).
8. Mandelbrot, B. B., Passoja, D. E. & Paullay, A. J. Fractal character of fracture surfaces of metals. *Nature* **308**, 721–722 (1984).
9. Shyam, A. & Milligan, W. Effects of deformation behavior on fatigue fracture surface morphology in a nickelbase superalloy. *Acta Mater.* **52**, 1503–1513 (2004).
10. Zhu, Q., Wang, C., Qin, H., Chen, G. & Zhang, P. Effect of the grain size on the microtensile deformation and fracture behaviors of a nickel-based superalloy via ebsd and in-situ synchrotron radiation x-ray tomography. *Mater. Charact.* **156**, 109875 (2019).
11. Zhao, Z. et al. A comprehensive study of the anisotropic tensile properties of laser additive manufactured Ni-based superalloy after heat treatment. *Int. J. Plast.* **148**, 103147 (2022).
12. Lv, P. et al. Temperature effects on tensile behaviors and relevant deformation mechanisms of a low-cost nickelbased single crystal superalloy containing 1.5% re. *J. Alloy. Compd.* **926**, 166819 (2022).
13. Gontard, L. et al. Assessment of engineered surfaces roughness by high-resolution 3D SEM photogrammetry. *Ultramicroscopy* **177**, 106–114 (2017).
14. Li, Y. et al. Multi-scale microstructural investigation of a laser 3D printed Ni-based superalloy. *Addit. Manuf.* **34**, 101220 (2020).
15. Eckmann, S. & Schweizer, C. Characterization of fatigue crack growth, damage mechanisms and damage evolution of the nickel-based superalloys mar-m247 cc (hip) and cm-247 lc under thermomechanical fatigue loading using in situ optical microscopy. *Int. J. Fatigue* **99**, 235–241 (2017).
16. Fukunaga, A. Differences between internal and external hydrogen effects on slow strain rate tensile test of ironbased superalloy a286. *Int. J. Hydrog. Energy* **47**, 2723–2734 (2022).
17. Kumar, P. et al. Compressive vs. tensile yield and fracture toughness behavior of a body-centered cubic refractory high-entropy superalloy al0.5nb1.25ta1.25tizr at temperatures from ambient to 1200 °C. *Acta Mater.* **245**, 118620 (2023).
18. Zhu, Q., Chen, G., Wang, C., Qin, H. & Zhang, P. Tensile deformation and fracture behaviors of a nickel-based superalloy via in situ digital image correlation and synchrotron radiation x-ray tomography. *Materials* **12**, 2461 (2019).
19. Liu, K. et al. In-situ X-ray tomography investigation of pore damage effects during a tensile test of a Ni-based single crystal superalloy. *Mater. Charact.* **177**, 111180 (2021).
20. Zhang, L., Sun, Z., Xue, Q., Lei, M. & Tian, X. Transient liquid phase bonding of ic10 single crystal with GH3039 superalloy using bni2 interlayer: microstructure and mechanical properties. *Mater. Des.* **90**, 949–957 (2016).
21. Kim, H., Cong, W., Zhang, H.-C. & Liu, Z. Laser engineered net shaping of nickel-based superalloy Inconel 718 powders onto aisi 4140 alloy steel substrates: interface bond and fracture failure mechanism. *Materials* **10**, 341 (2017).
22. Polcari, D., Dauphin-Ducharme, P. & Mauzeroll, J. Scanning electrochemical microscopy: a comprehensive review of experimental parameters from 1989 to 2015. *Chem. Rev.* **116**, 13234–13278 (2016).
23. Vernon-Parry, K. D. Scanning electron microscopy: an introduction. *III-Vs Rev.* **13**, 40–44 (2000).
24. Ding, W., Zhang, Y., Lu, H., Wan, W. & Shen, Y. Automatic 3D reconstruction of SEM images based on nanorobotic manipulation and epipolar plane images. *Ultramicroscopy* **200**, 149–159 (2019).
25. Eggeman, A. S., Krakow, R. & Midgley, P. A. Scanning precession electron tomography for three-dimensional nanoscale orientation imaging and crystallographic analysis. *Nat. Commun.* **6**, 7267 (2015).
26. Borzunov, A. et al. 3D surface topography imaging in SEM with improved backscattered electron detector: arrangement and reconstruction algorithm. *Ultramicroscopy* **207**, 112830 (2019).
27. Lu, J., Chen, B., Liu, X., Yang, F. & Robinson, I. K. 3D microstructure reconstruction of casting aluminum alloy based on serial block-face scanning electron microscopy. *J. Alloy. Compd.* **778**, 721–730 (2019).
28. Jung, J. M., Yoo, J. H., Jeong, H. J., Lee, S. & Kim, H. S. Three-dimensional characterization of sic particle-reinforced al composites using serial sectioning tomography and thermo-mechanical finite element simulation. *Mater. Trans. A* **45**, 5679–5690 (2014).
29. Yuan, H., Van de Moortele, B. & Epicier, T. Accurate post-mortem alignment for focused ion beam and scanning electron microscopy (FIB-SEM) tomography. *Ultramicroscopy* **228**, 113265 (2021).
30. Liu, K. et al. Effect of cooling rate on carbides in directionally solidified nickel-based single crystal superalloy: X-ray tomography and U-net CNN quantification. *J. Alloy. Compd.* **883**, 160723 (2021).
31. Verhoeven, G. Taking computer vision aloft-archaeological three-dimensional reconstructions from aerial photographs with photoscan. *Archaeol. Prospect.* **18**, 67–73 (2011).
32. Gontard, L. C., Schierholz, R., Yu, S., Cintas, J. & Dunin-Borkowski, R. E. Photogrammetry of the threedimensional shape and texture of a nanoscale particle using scanning electron microscopy and free software. *Ultramicroscopy* **169**, 80–88 (2016).
33. Barbieri, G. & da Silva, F. P. Acquisition of 3D models with submillimeter-sized features from SEM images by use of photogrammetry: a dimensional comparison to microtomography. *Micron* **121**, 26–32 (2019).
34. Sihvonen, T. & Reinikainen, S.-P. Image based evaluation of textured 3DSEM models. *Ultramicroscopy* **238**, 113518 (2022).
35. Tafti, A. P. et al. 3DSEM++: adaptive and intelligent 3D SEM surface reconstruction. *Micron* **87**, 33–45 (2016).
36. Eulitz, M. & Reiss, G. 3D reconstruction of SEM images by use of optical photogrammetry software. *J. Structural Biol.* **191**, 190–196 (2015).
37. Tondare, V. N. A concept for three-dimensional particle metrology based on scanning electron microscopy and structure-from-motion photogrammetry. *J. Res. Natl. Inst. Standards Technol.* **125**, 125014 (2020).
38. Tafti, A. P., Kirkpatrick, A. B., Alavi, Z., Owen, H. A. & Yu, Z. Recent advances in 3D SEM surface reconstruction. *Micron* **78**, 54–66 (2015).
39. Kozikowski, P. Extracting three-dimensional information from SEM images by means of photogrammetry. *Micron* **134**, 102873 (2020).
40. Li, L. et al. The effect of Al and Ti on the microstructure, mechanical properties and oxidation resistance of γ -Ni3 (Al, Ti) strengthened austenitic stainless steels. *J. Mater. Res. Technol.* **24**, 4650–4660 (2023).
41. Zhang, Z. et al. Microstructures and mechanical properties of a L12-structured precipitation strengthened Co-based superalloy. *J. Mater. Res. Technol.* **26**, 7789–7802 (2023).
42. Stinville, J. C. et al. High resolution mapping of strain localization near twin boundaries in a nickel-based superalloy. *Acta Mater.* **98**, 29–42 (2015).
43. Texier, D. et al. Strain localization in the Alloy 718 Ni-based superalloy: from room temperature to 650 °C. *Acta Mater.* **268**, 119759 (2024).
44. Gao, W. et al. Effect of grain size on deformation and fracture of Inconel718: an in-situ SEM-EBSD-DIC investigation. *Mater. Sci. Eng. A* **861**, 144361 (2022).
45. Chen, J. et al. In-situ study of adjacent grains slip transfer of Inconel 718 during tensile process at high temperature. *Int. J. Plast.* **163**, 103554 (2023).
46. Jacobs, S. D. Manipulating mechanics and chemistry in precision optics finishing. *Sci. Technol. Adv. Mater.* **8**, 153–157 (2007).
47. Yan, L., Rong, Y., Jiang, F. & Zhou, Z. X. Threedimension surface characterization of grinding wheel using white light interferometer. *Int. J. Adv. Manuf. Technol.* **55**, 133–141 (2011).
48. Darafon, A., Warkentin, A. & Bauer, R. Characterization of grinding wheel topography using a white chromatic sensor. *Int. J. Mach. Tools Manuf.* **70**, 22–31 (2013).

49. Tian, X. et al. Afm characterization of surface mechanical and electrical properties of some common rocks. *Int. J. Min. Sci. Technol.* **32**, 435–445 (2022).
50. Marturi, N., Tamadazte, B., Dembele, S. & Piat, N. Visual servoing-based approach for efficient autofocusing in scanning electron microscope. In *2013 IEEE/RSJ International Conference on Intelligent Robots and Systems*, 2677–2682 (2013).
51. Marturi, N., Tamadazte, B., Dembele, S. & Piat, N. Visual servoing-based depth-estimation technique for manipulation inside SEM. *IEEE Trans. Instrum. Meas.* **65**, 1847–1855 (2016).
52. Liu, H. et al. Influence of thermal exposure on microstructural stability and tensile properties of a new Ni-base superalloy. *J. Mater. Res. Technol.* **21**, 4462–4472 (2022).
53. Guillaume, R. et al. Impact of solute flow during directional solidification of a Ni-based alloy: in-situ and real-time X-radiography. *Acta Mater.* **177**, 111180 (2021).

Acknowledgements

This work has been supported by National Natural Science Foundation of China (No. 92367205), National Science and Technology Major Project of China (J2019-III-0008-0051), Basic Science Center Program for Multiphase Media Evolution in Hypergravity of the National Natural Science Foundation of China (No. 51988101), Zhejiang Provincial Natural Science Foundation of China under Grant LZ22F030011, Shanxi-Zheda Institute of Advanced Materials and Chemical Engineering (2022SZ-TD007). The supports are gratefully acknowledged.

Author contributions

X. Zhang, W.M., J.C., Z.Z. designed the research study. J.W., X. Zhao prepared and provided the specimens. X. Zhang, J.W. conducted in situ tensile experiments. X. Zhang, Z.L., S.H. implemented the method and wrote the code. X. Zhang, G.G., Y.Z. performed the analysis. X. Zhang, G.G., Z.L., W.M., Q.Y. wrote the paper. All authors read and approved the manuscript.

Competing interests

The authors declare no competing interests.

Additional information

Supplementary information The online version contains supplementary material available at <https://doi.org/10.1038/s44172-024-00257-6>.

Correspondence and requests for materials should be addressed to Wenchao Meng or Yuefei Zhang.

Peer review information *Communications Engineering* thanks E.S. Perdahcioglu and the other, anonymous, reviewer(s) for their contribution to the peer review of this work. Primary Handling Editors: Emanuela Bosco, Anastasiia Vasylichenko, Rosamund Daw. A peer review file is available.

Reprints and permissions information is available at <http://www.nature.com/reprints>

Publisher's note Springer Nature remains neutral with regard to jurisdictional claims in published maps and institutional affiliations.

Open Access This article is licensed under a Creative Commons Attribution-NonCommercial-NoDerivatives 4.0 International License, which permits any non-commercial use, sharing, distribution and reproduction in any medium or format, as long as you give appropriate credit to the original author(s) and the source, provide a link to the Creative Commons licence, and indicate if you modified the licensed material. You do not have permission under this licence to share adapted material derived from this article or parts of it. The images or other third party material in this article are included in the article's Creative Commons licence, unless indicated otherwise in a credit line to the material. If material is not included in the article's Creative Commons licence and your intended use is not permitted by statutory regulation or exceeds the permitted use, you will need to obtain permission directly from the copyright holder. To view a copy of this licence, visit <http://creativecommons.org/licenses/by-nc-nd/4.0/>.

© The Author(s) 2024